CO_2 and Temperature Induced Switching of a Flexible Metal-Organic Framework with Surface-Mounted Nanoparticles

Jan Berger,[†$] *Stephanie Terruzzi,*[§$] *Hana Bunzen,*[‡] *Marcello Marelli,*[ǂ] *Luca Braglia,*[⁑] *Roland A. Fischer,*[†] *Valentina Colombo,*[§ǂ]* *and Gregor Kieslich*[†]*

[†]Technical University of Munich, TUM School of Natural Sciences, Department of Chemistry, Lichtenbergstr. 4, 85748 Garching, Germany

[§]Department of Chemistry, University of Milan, Via Golgi 19, 20133 Milan, Italy

[*]INSTM, UdR Milano, Via Golgi 19, 20133 Milan, Italy

[‡]Institute of Physics, University of Augsburg, Universitätsstr. 1, 86159 Augsburg, Germany

[ǂ]CNR SCITEC - Istituto di Scienze e Tecnologie Chimiche “Giulio Natta”, Via Fantoli 16/15, 20138 Milan, Italy

[⁑] I CNR IOM – Istituto Officina dei Materiali, Laboratorio TASC, AREA Science Park, Basovizza, Trieste, 34149, Italy

[$]these authors contributed equally

ABSTRACT

The stimuli responsiveness of a material defines its potential application. Within the class of metal-organic frameworks (MOFs) the subclass of flexible MOFs (flexMOFs) has attracted great attention, showing large structural flexibility as a response to external stimuli such as guest adsorption, temperature, and pressure. Derived hybrid composites like nanoparticle (NP) loaded flexible MOFs, which stand to potentially combine advantageous properties of both are yet largely unexplored. Here we report the synthesis of flexible MOFs with surface mounted nanoparticles, e. g. NP@Zn_2(BME-bdc)$_2$dabco composites (NP = Pt and SiO_2 nanoparticles, BME-bdc^{2-} = 2,5-bismethoxyethoxy-1,4-benzenedicarboxylate, dabco = 1,4-diazabicyclo[2.2.2]octane), studying the impact of nanoparticles on the stimulus-responsiveness of a flexible MOF. We show that CO_2 physisorption triggered flexibility of the MOF is fully retained and reversible for all NP@flexMOF composites. Additionally, we observe that NPs stabilize the large pore state of the MOF, slightly increasing and shifting the switching pressure window. This effect is also observed during temperature-induced switching but Pt@flexMOF composites partially lose long-range order during the reversion to their narrow pore state, while attached SiO_2 NPs allow for a fully reversible transition. These findings suggest that the total exerted material strain triggering the switching is heavily dependent on NP size and the applied stimulus and that guest-induced switchability can be fully realized in NP@flexMOF hybrid materials.

INTRODUCTION

The study of a materials' stimuli responsiveness and its synthetic control is of great importance across a diverse range of research fields in material science. Metal-organic frameworks (MOFs) are well-known for their chemical versatility, featuring an intriguing platform for material design via targeted, chemical changes on the linker or metal node.[1] A subclass of MOFs, so-called flexible MOFs, exhibit both a variety of modes of response and activating stimuli.[2,3] Their most typical response is a change in accessible porosity by a phase transition from a contracted state (narrow/closed pore, **np**/**cp**) to an expanded state (large/open pore, **lp**/**op**), see Figure 1. Flexible MOFs are considered promising candidates for applications where dynamic guest capacity is exploited, *i.e.* gas storage and separation,[4,5] sensing,[6,7] drug release,[8,9] and switchable catalysis, [10] or where the phase transition is used as energetic sink, *i.e.* as shock absorber or damping materials.[11–13]

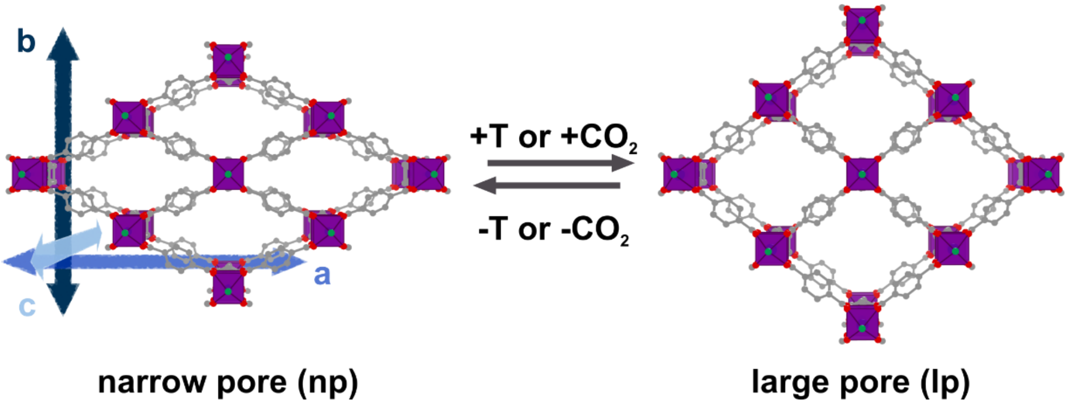

Figure 1. Visualization of $Zn_2(BME\text{-}bdc)_2dabco$ and directions of unit cell parameters a, b, and c. The MOF exhibits a switchable phase transition from its narrow pore (**np**) phase lozenge-lattice to its large pore (**lp**) phase square-lattice. View along the stacked dabco pillars in c direction. C, grey; O, red; N, green; Zn coordination polyhedron, purple; hydrogen atoms and BME functionalization of the bdc linker is not shown for clarity.

Focusing on switching behavior of flexible MOFs, guest adsorption and adsorbate concentration have been in the focus of many studies, including what are now considered prototypical flexible MOFs such as ELM-11,[14] MIL-53,[15] SNU-9,[16] or pillared-layered MOFs DUT-8 and $Zn_2(fu\text{-}bdc)_2dabco$,[17,18] to name just a few. Today, the use of adsorbate controlled switching has been demonstrated in, for example, high-throughput separation in pressure vacuum swing adsorption of methane and CO_2,[19] ternary sieving of ethane, ethylene and CO_2,[20] variable-aperture porous organic cage membranes for graded molecular sieving,[21] isotope-responsive breathing,[22] or solvent-induced control over separation selectivity.[23] Additionally, other external stimuli have been explored such as temperature, mechanical pressure and electric fields. For electric-field induced phase transitions only a few reports exists,[24,25] while temperature and mechanical pressure have shown to be suitable stimuli for switching between the **np** and **lp** form in materials such as ZIF-4, MIL-53 and its derivates, and members of the series $[M(fu\text{-}bdc)_2dabco]$.[3,26,27] Additionally, studies on systems such as linker-functionalized MOF-5 derivates[28] and $[Cu(DB\text{-}bdc)_2dabco]$[29] have highlighted the complex interplay between enthalpic and entropic interactions that cause trigger-induced structural flexibility. Here, we would like to highlight the contribution of several theoretical studies on this topic, which, in synergy with experimental works, helped to step-wise carve out a clearer picture of the structure-chemical factors that determine flexibility in MOFs.[27,30–32]

Apart from switchable phase transitions, almost all conceivable stimuli can be applied to induce changes in linker conformation,[24,33–35] redox states,[36–38] optical properties,[39–41] or conductivity.[42] Therefore, it is surprising that understanding of the impact of nanoparticles (NP) on MOF flexibility - whether they are incorporated into the bulk or mounted on the surface - is yet a largely unexplored area. It has been found that linker rotation can influence conversion and selectivity for Pt@ZIF-8 materials used in catalysis;[43] however, to the best of our knowledge the inverse question of how flexibility in MOFs is affected by NPs has not been investigated outside of a recent study from us where we focused on the thermal expansion properties of Pt@MOF composites.[44]

The research areas of NP loaded MOF materials and switchable, flexible MOFs are yet not interlinked while scenarios in which network switching regulates catalysis conditions at the NPs, and in which NPs direct framework switching behavior can easily be envisioned. Therefore, we see great potential in forming this link. In this pursuit, we here explore how NPs impact framework switchability and investigate the influence of surface-mounted Pt and SiO_2 NPs and type of stimulus (guest, temperature) on the phase transition of the functionalized, flexible pillared-layered model system Zn_2(BME-bdc)$_2$dabco, see Figure 1 and supporting information S1.5 for details of the parent MOF structure. We compare an isoreticular series of Pt@Zn_2(BME-bdc)$_2$dabco composites with different Pt loading, a SiO_2@Zn_2(BME-bdc)$_2$dabco composite, and a well-studied NP-free reference. The results suggest that guest-induced switching is maintained and facilitated in NP@MOF composites while the reversibility of temperature-induced phase transitions is heavily affected by smaller metal NPs.

METHODS

Material synthesis. Chemicals were purchased from commercial suppliers (Sigma-Aldrich, Alfa Aesar, ABCR and others) and used without further purification. SiO_2 NPs were purchased from Micromod GmbH (Germany). Ethanol for solvent exchange was purchased as technical grade and redistilled prior to use. The linker was synthesized via etherification according to optimized literature known procedures (see S1.2).[45] Pt@Zn_2(BME-bdc)$_2$dabco composites were synthesized via a concerted one-pot crystallization of MOF and formation of Pt NPs without any capping agents.[46] This method combines the solvothermal MOF synthesis in dimethylformamide (DMF),[47] with a solvent mediated Pt^{2+} reduction. SiO_2@Zn_2(BME-bdc)$_2$dabco composites were synthesized by adding a stable colloidal dispersion of pre-formed NPs to the reaction mixture during solvothermal MOF synthesis. See supporting information S1.3 for full details.

Analytical methods. Liquid state NMR spectra were measured on a Bruker Ultrashield DRX400 at ambient temperature, for details see supporting information S1.1. For the measurements, MOF samples were digested and subsequently measured in DMSO-d_6 with DCl, organic linkers were dissolved and measured in DMSO-d_6. CHNS contents were determined via combustion analysis. Powder X-ray diffraction (PXRD) patterns of the as-synthesized (**as**) samples were measured on a Rigaku Benchtop MiniFlex 600-C (X-ray Cu Kα radiation, λ = 1.5418 Å). Samples were measured in activated (**dry**) state and after physisorption measurements in sealed capillaries with Debeye-Scherrer geometry on a PANalytical Empyrean (X-ray Cu Kα radiation, λ = 1.5418 Å), for further details see supporting information S2. Adsorption measurements were carried out on a 3Flex Physisorption Instrument by Micromeritics Instrument Corp. Samples were activated at 80 °C for 5 h under dynamic vacuum using a SmartVacPrep by Micromeritics Instrument Corp. to ensure absence of unwanted adsorbates. The adsorbent mass was then recorded, generally in the range of 50-70 mg, for more method details see supporting information S3. All adsorption isotherms are accessible online free of charge as adsorption information files to counter issues with post-publishing adsorption data extraction and facilitate machine learning, see supporting information.[48] Thermogravimetric analysis coupled with differential scanning calorimetry (TGA-DSC) was conducted on a Netzsch TG-DSC STA 449 F5 in a temperature range from 25 to 800 °C under argon flow, for details see supporting information S4. Variable temperature PXRD (VT-PXRD) measurements were performed using a custom-made sample heater plugged in a Bruker AXS D8 Advance diffractometer (X-ray Cu Kα radiation, λ = 1.5418 Å) with Bragg-Brentano geometry (see S5). About 10 mg of sample were deposited in a background free sample-holder (a properly misoriented quartz single crystal) and heated in air from 30 °C up to 290 °C with steps of 20 °C. Scanning transmission electron microscopy (STEM) with energy dispersive X-ray spectroscopy (EDS) elemental mappings of **B1-3** were recorded with a JEM-ARM200F "NEOARM" microscope from JEOL (Germany) GmbH with a cold FEG electron source operated at 200 kV. Transmission electron microscopy (TEM) micrographs of sample **B4** were recorded on a ZEISS LIBRA200FE equipped with a Schottky FEG electron source operated at 200 kV. Samples were prepared by depositing a drop of the solid dispersed in 2-propanol onto lacey carbon copper grids (300 mesh) and dried in air, see supporting information S7. X-ray photoemission spectra (XPS) of sample **B3** were recorded using a conventional non-monochromatized X-ray source (Al Kα radiation, λ = 8.3896 Å) with a hemispherical electron energy analyzer in a dedicated chamber of the NFFA UHV MBE-cluster system.[49] The Pt 4f and Zn 2p spectra have been acquired using a pass energy of 50, a dwell time of 500 ms and a channel width of 1.1 mm, see supporting information S8.

RESULTS AND DISCUSSION

NP@MOF composite synthesis. The NP@MOF composites investigated in this study involve either Pt or SiO_2 NPs. Pt NPs were chosen due to known experimental accessibility of small Pt NPs (< 5 nm) by reduction of Pt^{2+} precursors, while SiO_2 NPs were chosen because of commercial availability of SiO_2 NPs in the desired regime of approximately 30 nm. Pt@Zn_2(BME-bdc)$_2$dabco composites were synthesized using a co-crystallization approach which is a one-step, one-pot crystallization of MOF and formation of surface mounted Pt NPs. In a typical reaction, all precursor materials, e. g. $Zn(NO_3)_2$, dabco, H_2BMEbdc (2,5-bismethoxyethoxy-1,4-benzene dicarboxylic acid) and K_2PtCl_4, are suspended in dimethylformamide (DMF). During solvothermal reaction, DMF is oxidized to its carbamic acid derivative in the presence of water which comes from trace amounts in the DMF and the hydrated metal salt. In parallel, Pt^{2+} is reduced to Pt^0 which facilitates NP formation.[50] Following this strategy, the MOF compound precipitates with the nanoparticles in the form of a composite. We would like highlight that this synthetic route avoids the use of capping agents during NP formation, which facilities reproducibility of the obtained composite materials.[51] More generally, this approach can be applied to create Pt@MOF composites in which Pt NPs are integrated into the bulk of a MOF by forming Pt *in situ* inside its pores.[46] In this work, we discovered that the functionalization of the MOF Zn_2(BME-bdc)$_2$dabco presumably inhibits sufficient reagent diffusion and therefore spatial proximity of oxidizing and reducing species within the pores, which prevents NP formation within the pore space. Instead, MOF particles crystallize, and Pt precursor reduction takes place predominantly outside the pores. Formed Pt NPs are then attached to the external surface of the MOF particles to yield Pt@ Zn_2(BME-bdc)$_2$dabco composites. The series of isoreticular functionalized Pt@MOF comprises of four materials based on Zn_2(BME-bdc)$_2$dabco with differing amounts of Pt NPs attached to the MOF surface (0, 1.1, 2.0, 2.8 wt%, see Table 1).

Table 1. Overview of the synthetized NP@Zn_2(BME-bdc)$_2$dabco materials used in this work along with the main compositional features of the five samples.

Material	NP	wt.%	size [nm]	surface funct.
B0	none	-	-	-
B1	Pt	1.1[a]	< 3	none
B2	Pt	2.0[a]	< 3	none
B3	Pt	2.8[a]	< 3	none
B4	SiO_2	1[b]	30	none

[a]per atom absorption spectroscopy and photometry; [b]calculated from added colloidal suspension

Besides these, we further synthesized a SiO_2@Zn_2(BME-bdc)$_2$dabco composite with the aim of comparing the most pronounced differences occurring in the composites when changing the NP size and type (see Table 1). This composite was prepared, similar to the bottle-around-a-ship method,[52] by adding a commercially available, stable colloidal aqueous dispersion of SiO_2 nanoparticles (30 nm, see Table S2 for specifications) to the educt mixture during solvothermal MOF synthesis. This allows the NPs to stick to the growing MOF crystal external surfaces.

All composites were washed, solvent exchanged, and activated which was verified with respect to MOF composition and solvent removal by ^{1}H NMR spectroscopy and TGA (see Figure S1). Pt content in samples **B1-3** was determined by atom adsorption spectroscopy and photometry. SiO_2 loading was calculated based on educt concentrations and marks the maximum wt.% value expected. More direct determination of the very low SiO_2 concentration in the composite was outside reliable and reproducible analytical capabilities. The parent Zn_2(BME-bdc)$_2$dabco is known to exhibit guest induced flexibility triggered by polar solvents/adsorbates such as DMF or CO_2.[45] The material is built from a 2D **sql** network spanned by the linker molecules and metal nodes which are stacked along the third dimension by dabco pillars, see Figure 1 and supporting information S1.5. The phase transition of this MOF is related to the contraction of the 2D square-network to a lozenge-network which comes with the change of pore space, i. e. switches between a large pore (**lp**) and narrow pore (**np**) state as shown in Figure 1. This structural deformation is generally referred to as wine-rack motion or breathing and often found in flexible MOFs with this topology.[2] PXRD confirms that all materials **B0** – **B4** are isostructural, independent of the NPs (Pt

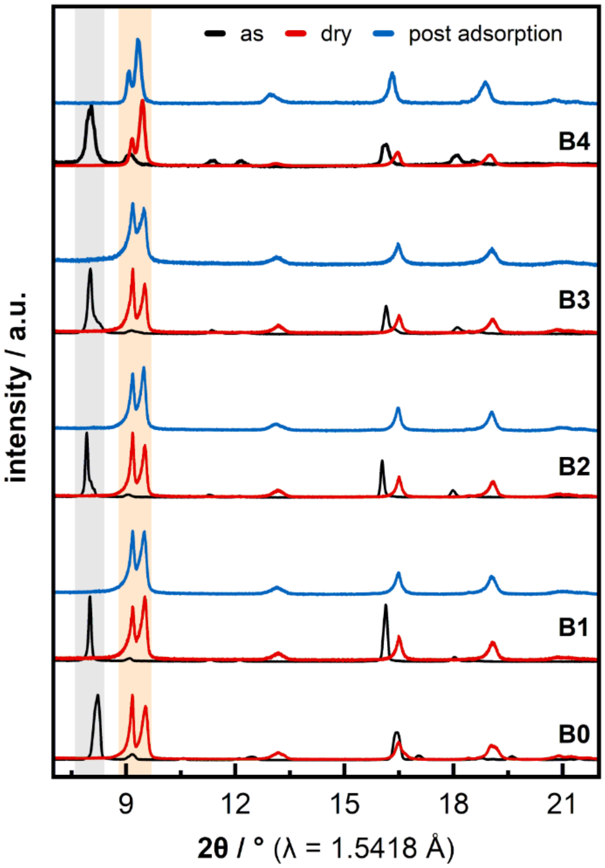

Figure 2. PXRD patterns of **B0-4** acquired in the range of 2θ = 7-22°. Transition from **lp** in the **as** form to **np** in the **dry** form is observable by the shift of the 110 reflection from 2θ = 8.0-8.4° (highlighted in grey) to 9.5-9.7° and intensity increase of the 001 reflection at 2θ = 9.2° (both highlighted in orange). Black trace, **as** (**lp** form); red trace, **dry** (**np** form); blue trace, same sample measured after all gas adsorption experiments.

or SiO_2) content. Importantly, this observation holds for the as-synthesized (**as**) **lp** state, which refers to the composites directly after synthesis, and the activated (**dry**), **np** state, which refers to the composites after solvent removal, see Figure 2. We note that Pt NPs are not observed in diffraction patterns due to the very low NP loading and significant peak broadening coming from diffraction domains in the nano regime (see Figure S1).

Nanoparticle allocation. The size, distribution and location of Pt nanoparticles were investigated by scanning transmission electron microscopy (STEM). The presence of Pt could be detected in samples **B1-3** by annular dark-field (ADF) STEM. Due to the difference in electron density between Pt nanoparticles and MOF, the Pt nanoparticles could be localized by contrast differences,

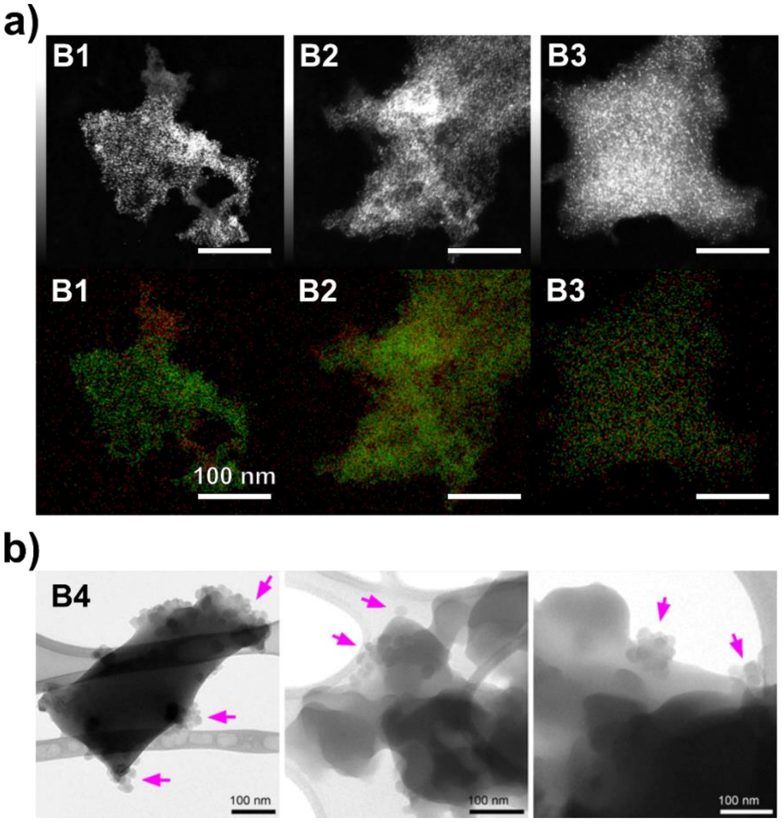

Figure 3. a) samples **B1-3** with Pt NPs. Top row: ADF-STEM images with heavier elements in brighter white, showing Pt visible as bright dots distributed across the sample. Bottom row: EDS-STEM image overlays (red, Zn; green, Pt; contrast adjusted for visibility) of the same crystals showing Pt predominantly on top of the MOF. All samples show heavy electron beam related degradation. Scale bars are 100 nm. b). TEM micrographs of sample **B4** -SiO_2 NPs onto MOF crystals support. Magenta arrows highlight the spherical SiO_2 NPs. Scale bars are 100 nm.

see **Figure 3**. To further validate the presence of the Pt nanoparticles and to study their distribution, elemental mapping based on energy dispersive X-ray spectroscopy (EDS) was carried out. Both results are shown in Figure 3a and section S7. In all three samples we detected Pt nanoparticles of approximately 1 - 3 nm with relatively homogenous particle distribution on the MOFs surface and only limited aggregation. During the measurement we observed strong degradation of the samples in the electron beam which is a known challenge for electron microscopy of MOFs. Therefore, Electron tomography (ET) which would provide depth-resolution was not successful. Previous work on the related composite system Pt@Zn_2(DP-bdc)$_2$dabco (DP-bdc^{2-} = 2,5-dipropoxy-1,4-benzene dicarboxylate), which allowed for ET to locate Pt NPs, show clearly that Pt NPs anchor on the outer MOF particle surface exclusively.[44] Together with the STEM and EDS results this indicates NPs of **B1-3** are predominantly attached to the surface of the MOF. Dispersion of the

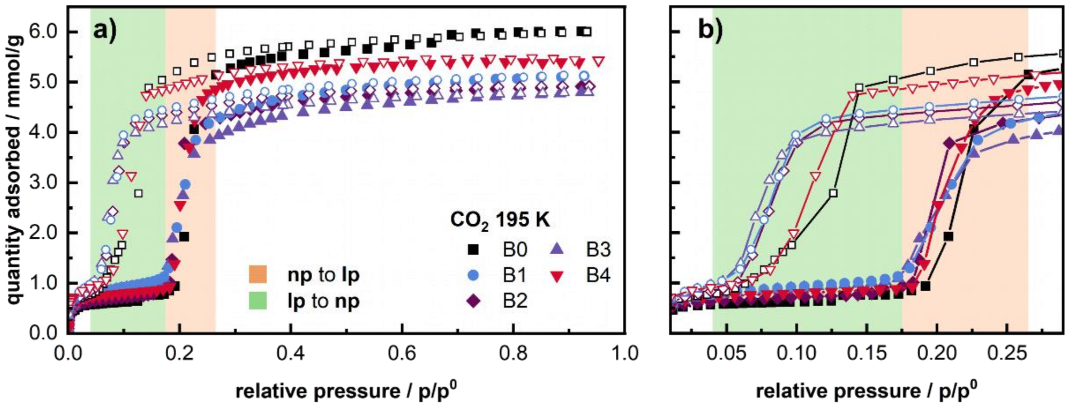

Figure 4. a) CO_2 physisorption isotherms of **B0-4**. Steps in the isotherms correspond to framework opening during adsorption (**np** to **lp**, light orange) and closing during desorption (**lp** to **np**, green). b) Highlighted pressure range of the low-pressure region, where the phase transitions occurs. Adsorption and desorption depicted in full and open symbols, respectively; lines have been added as visual aid only.

SiO_2 nanoparticles of composite **B4** were investigated using transmission electron microscopy (TEM). The preformed nanoparticles are bigger and thus easier to detect despite the decrease in contrast, see Figure 3b. The size-ratio of MOF particles (ca. 300-500 nm) to SiO_2 NPs (30 nm) practically excludes NP incorporation in the MOF's pores. The SiO_2 NPs tend to aggregate and attach onto the MOF surface, assembling into a stable nanocomposite system. Notably, all STEM and TEM micrographs have been performed on samples subjected to extensive washing and activation (see ESI for details) confirming that both types of NPs are properly attached to their MOF supports. We further note that changes in NP concentration do not notably affect MOF particle size which otherwise could have an impact on MOF flexibility.[53]

Guest-induced switching. $Zn_2(BME\text{-}bdc)_2dabco$ is known to be non-porous towards nitrogen and exhibits a reversible CO_2 adsorption induced phase transition from the **np** to the **lp** phase.[45] Physisorption experiments performed on the our reference sample (**B0**) and the NPs composites show that this behavior is fully retained in all NP@MOF (**B1-4)** composites as evidenced by their stepped CO_2 physisorption isotherms, see Figure 4a. Furthermore, all materials are non-porous towards nitrogen, see Figure S2. Additionally, we have collected PXRD pattern of all compounds after CO_2 desorption, see Figure 2 blue pattern, confirming that reversibility is related to maintaining framework integrity.

Composites **B1**, **B2**, and **B3** show a Pt content dependent linear decrease of total absolute uptake of 15 - 25 % when compared to the reference material **B0**. A small part of the uptake reduction can be attributed to the composites' mass increase due to Pt NPs without contributing to porosity, therefore decreasing the uptake to mass ratio. In light of the low mass percentage of the Pt NPs, most of the capacity decrease presumably results from NP-induced porosity changes to the underlying MOF phase. The phase transition pressure for framework opening and closing, see Figure 4b, are shifted to lower pressures in **B1-3** compared to **B0**. This is rationalized by Pt NPs interacting with the MOF particles during their initial crystallization, which occurs in the **lp** phase. Presumably, this results in a stabilizing contribution for the **lp** form and therefore a lower gas pressure for triggering the **np**-to-**lp** phase transition. The same trend we observe for the **lp**-to-**np** phase transition during desorption; however, the in the desorption cycle is even slightly larger. The bigger, surface-mounted SiO_2 nanoparticles in **B4** also lead to a minor total uptake decrease and shifting of both phase transitions during adsorption and desorption to slightly lower pressures; however, the effect is less pronounced compared to the Pt NPs and indicates the SiO_2 NPs exert a less rigidifying and pore-blocking effect on the MOF support. We correlate this to the intuitive factors of NP size and absolute amount, where a larger number of smaller NPs exhibits more strain on the support than a lower number of bigger NPs. Intriguingly, parallels can be drawn to flexible MOFs anchored to surfaces where this effect is put to the extreme: a decreased thin film thickness, and therefore a larger ratio of anchored external surface area, which here translates to a larger NP coverage, leads to significantly reduced adsorbate-induced flexibility, i. e. a stabilization of the lp phase.[54]

Overall, porous and guest-switchable NP@MOF composites with low loadings of small Pt NPs and bigger SiO_2 NPs can be realized. The change in bulk material property directed by surface-mounted NPs is conceptually similar to surface-defect altered flexibility in MOFs.[55,56] This can be rationalized especially in light of a recent study by Thompson et al.[53] Therein, they investigate the particle size-dependent flexibility of DUT-8 (Zn_2ndc_2dabco, ndc^{2-} = 2,6-naphthalene dicarboxylate, Dresden University of Technology) also concluding that it is the concentration and amount of surface defects and related nucleation barriers of the phase transition that govern material flexibility, rather than the particle size. In our NP@flexMOF composites, the NPs can be seen as defect-generating agents, and it is reasonable to assume, that their absolute amount is more influential than their size, thus making this the main reason for the observed differences between sample **B1-3** and **B4**.

Thermal responsiveness. In addition to flexibility towards CO_2 adsorption, Zn_2(BME-bdc)$_2$dabco is known to exhibit a reversible, temperature-triggered **np** to **lp** phase transition at approximately $T = 210$ °C.[47] Before analyzing the impact of Pt and SiO_2 NPs on the temperature responsiveness, all composites were analyzed by thermogravimetric analysis coupled with differential scanning calorimetry (TGA-DSC), see supporting information S4. TGA under inert gas flow shows that all Pt containing composites decompose approximately 50 °C earlier than the NP free reference **B0**, T_{dec}(B0) = 269 compared to T_{dec}(B1) = 225 °C, T_{dec}(B2) = 219 °C and T_{dec}(B3) = 223 °C. In contrast, **B4** is thermally as stable as **B0**, T_{dec}(B4) = 271 °C. The DSC traces also show that all composites materials exhibit phase transitions at 210 °C (**B1-3**) or 215 °C (**B4**). This is in good agreement with literature, but 10 °C and 5 °C below our reference material **B0**, see Figure S3.[47] Qualitatively, this already indicates that NP@MOF composites with both Pt and Si NP still exhibit a temperature-driven **np**-to-**lp** phase transition, while Pt nanoparticles are anticipated to have bigger impact on the temperature responsive behavior compared to Si. In order to investigate structural changes and the reversibility of these phase transitions in more detail, variable temperature powder X-ray diffraction (VT-PXRD) experiments were conducted for all composites. Samples were subjected to an *in situ* heating and cooling cycle from 30 to 290 °C and back to 30 °C at ambient air, with diffraction patterns collected every 20 °C. The results are shown in Figure 5a and Figure S4. Moreover, unit cell parameters derived from Le Bail refinements have been determined and are reported in Figure 5b and section S6, and more details of the fitting procedures are given in the supporting information S6.

The expected and characteristic structural response of the reference material **B0** can directly be observed from Figure 5a. Starting from room temperature, a temperature increase triggers the **np**-to-**lp** phase transition at approximately $T = 290$ °C where the strong intensity reflection of the (110) plane between $2\theta = 8 - 8.4°$ is indicative. During cooling, the phase transition occurs less abrupt and is only finished at approximately $T = 220$ °C, which is also reflected in the extracted lattice parameters, see Figure 5b. The differences in absolute temperature of the transition temperature compared to TGA-DSC data and literature[47] is attributed to the different experimental conditions of VTPXRD experiments, where the impact of atmosphere (air compared to inert atmosphere) presumably leads to the largest difference, see ESI for details. The onset temperatures

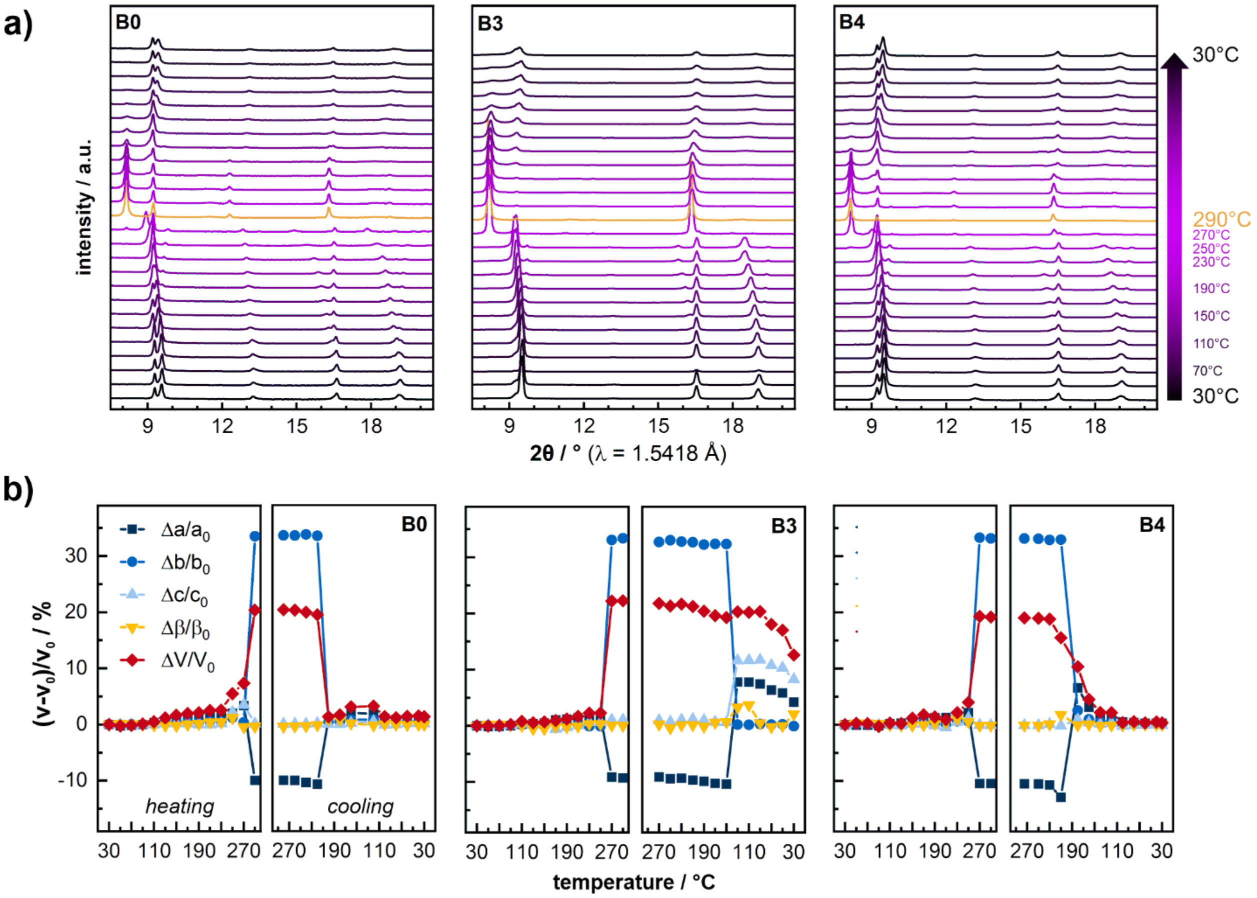

Figure 5. a) VT-PXRD pattern series collected during the heating/cooling cycle experiment comparing the reference material (**B0**, left), the composite with the highest Pt nanoparticle loading (**B3**, middle), and the SiO_2@MOF composite (**B4**, right) in the range of $2\theta = 7.5\text{-}20.5°$. Patterns at highest temperature are highlighted in orange. For **B1** and **B2** see Figure S4. b) Relative percentage variation of the unit cell parameters (v) with respect to the values at 30 °C (v_0), before heating.

of the phase transition for **B1-4** show a similar trend as results from DSC, i. e. an earlier framework opening to the **lp** phase during heating. Again the (110) reflection is indicative for a qualitative analysis, while extracted lattice parameters confirm this trend quantitatively, see Figure 5b. The thermally induced **np**-to-**lp** transition occurs in all composites, irrespective of NP type or loading. The anisotropic unit cell parameter changes, i. e. the increase of the *b* axis, decrease of the *a* axis, and only very little changes in the *c* axis and of the β angle, correspond to the wine-rack opening motion which changes the **np** lozenge-structure to the **lp** square-tye structure, see Figure 1. Interestingly, the closing **lp**-to-**np** transition during cooling is slightly delayed for all NP@MOF composites, when compared to the parent **B0** pure MOF. Indeed, **B4** turns back to the **np** phase at ca. 210 °C, that is about 10 °C after **B0**, while the Pt@MOF materials largely revert to their **np** phase at 190 °C (**B1**), 170 °C (**B2**), and 150 °C (**B3**).

The broadened hysteresis in the temperature-induced switching indicates that the surface-attached NPs stabilize the **lp** form of the MOF once it is in this phase. This effect is similar to what has been observed for CO_2 as a stimulus and is slightly stronger for Pt than SiO_2 nanoparticles. A key difference relates to the reversibility of the phase transition. Full reversibility is only observed for SiO_2-based composites, while composites with Pt NPs show a significantly peak broadening related to the main reflections of the **np** phase, see Figure 5a. Raw pattern of **B3** after heating show a residual (110) reflection of the **lp** phase down to 70 °C, and the incoherencies of the extracted lattice parameters related to a lower accuracy of the Le Bail profile fits due to peak broadening and intensity loss reflect this partial reversibility. Therefore, a loss of long-range order after the first heating cycle is observed for Pt@MOF composites, which is pronounced for composites with larger Pt content, see Figure S4. This behavior during temperature-induced framework closing is in contrast to the fully reversible CO_2-induced phase transition of these Pt@MOF composites where the crystallinity of the phase transition is retained. This difference suggests a combined influence of the platinum nanoparticles and high temperatures on the MOFs' switchability. To test if Pt NPs could be oxidized under measurement conditions (in air) and then react with the MOF support to facilitate its degradation and to confirm the oxidation state of the Pt NPs prior and after the thermal treatments, X-ray photoelectron spectroscopy (XPS) measurements on the **B3** sample prior and after VT-PXRD experiments. The results of the XPS measurements are shown in Figure S8 and confirms identical oxidation state of the Pt NPs for both as synthesized and thermally treated sample. Interestingly, the intensity of Pt 4f core level diminishes after the thermal treatment, while the overall spectrum shape remains unchanged (see Figure S8, comparison with unaltered Zn 2p core level). This behavior can be explained by migration of Pt NPs from the surface to the pores or to some aggregation effect of the Pt NPs, resulting in a minor registered intensity of the Pt 4f. Overall, this suggests that size and amount of surface-mounted nanoparticles dominate rather than chemical identity, and the effect of NPs on the temperature reduced switching behavior is mechanical in nature rather than related to its chemical identity, similar to what has been observed for CO_2 as stimuli.

CONCLUSION

Motivated by the scope that NP offer in altering switchability of flexible MOFs and adding potential catalytic functionality, we successfully synthesized such composites consisting of mesoscopic platinum or silicon dioxide nanoparticles surface-mounted to the flexible MOF $Zn_2(BME\text{-}bdc)_2dabco$. We compared CO_2-adsorption and thermally induced switching for three Pt@MOF composites (1, 2, and 3 wt.% Pt) and one SiO_2@MOF composite to the pure, flexible MOF. For both stimuli we observe that Pt NPs stabilize the **lp** form. Physisorption experiments show that CO_2-switchability is retained and fully reversible for all composites. Full reversibility related to structural stability is only given for CO_2-induced switching, while temperature-induced switching leads to significant reduction of crystallinity during the first cycling for Pt@MOF composites. In contrast, fewer, bigger NPs in the SiO_2@MOF composite displays reversible switching with fully retained framework crystallinity. We primarily connect this to the absolute NP amount attached to the surface, which is higher for smaller NPs at comparable loadings, and therefore results in higher strain exerted onto the MOF support in addition to the thermal stress at higher temperatures. Moreover, migration of the small Pt NPs to the MOFs' pores during thermal treatment can be also considered as explanation of such effect, potentially indicating that small metal NPs can acts as defect-directing agents in NP@MOFs composites.

Fundamentally, it is highly encouraging for future research in this direction that low loadings of surface-mounted nanoparticles do not necessarily compromise flexibility (and porosity) of MOFs. Nanoparticle type, size and loading do affect the strain exerted on the MOF, as we indirectly observed in physisorption and VT-PXRD experiments, but moreover the type of stimulus (or strain) used to switch the framework state plays an equally important role. The apparent common ground is the stabilization of the **lp** phase by NPs which could be of more general use for widening the pressure or temperature windows open/large pore phases of flexible MOFs are favored in, as well as changing the point of framework opening to lower pressures or temperatures. Within this focused study we aimed to probe for and highlight this correlation, and we envision future studies expanding on both sets of nanoparticle-related and stimuli-specific contributions to switchability behavior. Understanding this will stepwise allow the transfer and combination of the extensive knowledge on flexible MOFs and NP@MOF composites for potentially both design versatility of each material class and new hybrid materials.

ASSOCIATED CONTENT

Supporting Information. Synthesis procedures; ^{1}H NMR spectra information; elemental analysis; TGA-DSC; PXRD data; N_2 and CO_2 physisorption isotherms; VT-PXRD data; Le Bail profile fit analysis; electron microscopy micrographs; XPS data and further information.

The following files are available free of charge.

Adsorption information files (ZIP)

AUTHOR INFORMATION

Corresponding Authors

*E-mail: valentina.colombo@unimi.it, gregor.kieslich@tum.de

ORCID

Jan Berger: https://orcid.org/0000-0002-9230-0398

Roland A. Fischer: https://orcid.org/0000-0002-7532-5286

Stephanie Terruzzi: https://orcid.org/0000-0003-4964-2891

Hana Bunzen: https://orcid.org/0000-0003-1824-0291

Marcello Marelli: https://orcid.org/0000-0003-3662-7326

Luca Braglia: https://orcid.org/0000-0003-0796-3670

Valentina Colombo: https://orcid.org/0000-0003-0263-4456

Gregor Kieslich: https://orcid.org/0000-0003-2038-186X

Author Contributions

J.B. performed Pt@MOF material synthesis, analysis, data processing, and manuscript writing. S.T. performed SiO_2@MOF material synthesis, analysis, data processing, and Le Bail profile fitting. H.B. performed electron microscopy and its visualization. M.M. performed energy-filtered electron microscopy and its visualization. L.B. performed XPS experiments and data processing. V.C. provided the motivation of this work and contributed to data processing. G.K. provided the motivation of this work and contributed to data processing. R.A.F. provided the motivation of this work. All authors contributed to manuscript writing and have given approval to the final version of the manuscript.

Notes

The authors declare no competing financial interests.

ACKNOWLEDGMENT

This work was funded by the DFG (Deutsche Forschungsgesellschaft; German Research Foundation) via the research unit FOR 2433 (MOF Switches). XPS measurements were performed within the Nanoscience Foundry and Fine Analysis (NFFA-MIUR Italy Progetti Internazionali) project. V.C. thanks the Italian MUR for funding through the PRIN2017 program (project 'Moscato' n° 2017KKP5ZR_004) and Università degli Studi di Milano for the Transition Grant (PSR2015-1721VCOLO_01).

REFERENCES

1 R. Freund, S. Canossa, S. M. Cohen, W. Yan, H. Deng, V. Guillerm, M. Eddaoudi, D. G. Madden, D. Fairen-Jimenez, H. Lyu, L. K. Macreadie, Z. Ji, Y. Zhang, B. Wang, F. Haase, C. Wöll, O. Zaremba, J. Andreo, S. Wuttke and C. S. Diercks, 25 Years of Reticular Chemistry, *Angew. Chem., Int. Ed.*, 2021, **60**, 23946–23974.

2 S. Seth and S. Jhulki, Porous flexible frameworks: origins of flexibility and applications, *Mater. Horiz.*, 2021, **8**, 700–727.

3 A. Schneemann, V. Bon, I. Schwedler, I. Senkovska, S. Kaskel and R. A. Fischer, Flexible metal-organic frameworks, *Chem. Soc. Rev.*, 2014, **43**, 6062–6096.

4 Y. Li, Y. Wang, W. Fan and D. Sun, Flexible metal-organic frameworks for gas storage and separation, *Dalton Trans.*, 2022.

5 M. Bonneau, C. Lavenn, J.-J. Zheng, A. Legrand, T. Ogawa, K. Sugimoto, F.-X. Coudert, R. Reau, S. Sakaki, K.-I. Otake and S. Kitagawa, Tunable acetylene sorption by flexible catenated metal-organic frameworks, *Nat. Chem.*, 2022.

6 Z. Zhai, X. Zhang, X. Hao, B. Niu and C. Li, Metal–Organic Frameworks Materials for Capacitive Gas Sensors, *Adv. Mater. Technol.*, 2021, **6**, 2100127.

7 L.-T. Zhang, Y. Zhou and S.-T. Han, The Role of Metal-Organic Frameworks in Electronic Sensors, *Angew. Chem., Int. Ed.*, 2021, **60**, 15192–15212.

8 J. W. M. Osterrieth and D. Fairen-Jimenez, Metal-Organic Framework Composites for Theragnostics and Drug Delivery Applications, *Biotechnol. J.*, 2021, **16**, e2000005.

9 Y. Zhou, T. Yang, K. Liang and R. Chandrawati, Metal-organic frameworks for therapeutic gas delivery, *Adv. Drug. Deliv. Rev.*, 2021, **171**, 199–214.

10 S. Yuan, L. Zou, H. Li, Y.-P. Chen, J. Qin, Q. Zhang, W. Lu, M. B. Hall and H.-C. Zhou, Flexible Zirconium Metal-Organic Frameworks as Bioinspired Switchable Catalysts, *Angew. Chem.*, 2016, **55**, 10776–10780.

11 X. Zhou, Y.-R. Miao, W. L. Shaw, K. S. Suslick and D. D. Dlott, Shock Wave Energy Absorption in Metal-Organic Framework, *J. Am. Chem. Soc.*, 2019, **141**, 2220–2223.

12 I. Beurroies, M. Boulhout, P. L. Llewellyn, B. Kuchta, G. Férey, C. Serre and R. Denoyel, Using pressure to provoke the structural transition of metal-organic frameworks, *Angew. Chem., Int. Ed.*, 2010, **49**, 7526–7529.

13 P. Iacomi, J. S. Lee, L. Vanduyfhuys, K. H. Cho, P. Fertey, J. Wieme, D. Granier, G. Maurin, V. van Speybroeck, J.-S. Chang and P. G. Yot, Crystals springing into action: metal-organic framework CUK-1 as a pressure-driven molecular spring, *Chem. Sci.*, 2021, **12**, 5682–5687.

14 A. Kondo, N. Kojima, H. Kajiro, H. Noguchi, Y. Hattori, F. Okino, K. Maeda, T. Ohba, K. Kaneko and H. Kanoh, Gas Adsorption Mechanism and Kinetics of an Elastic Layer-Structured Metal–Organic Framework, *J. Phys. Chem. C*, 2012, **116**, 4157–4162.

15 T. Loiseau, C. Serre, C. Huguenard, G. Fink, F. Taulelle, M. Henry, T. Bataille and G. Férey, A rationale for the large breathing of the porous aluminum terephthalate (MIL-53) upon hydration, *Chemistry*, 2004, **10**, 1373–1382.

16 H. J. Park and M. P. Suh, Stepwise and hysteretic sorption of N(2), O(2), CO(2), and H(2) gases in a porous metal-organic framework Zn(2)(BPnDC)(2)(bpy), *Chem. Commun.*, 2010, **46**, 610–612.

17 N. Klein, H. C. Hoffmann, A. Cadiau, J. Getzschmann, M. R. Lohe, S. Paasch, T. Heydenreich, K. Adil, I. Senkovska, E. Brunner and S. Kaskel, Structural flexibility and

intrinsic dynamics in the M2(2,6-ndc)2(dabco) (M = Ni, Cu, Co, Zn) metal–organic frameworks, *J. Mater. Chem.*, 2012, **22**, 10303.

18 S. Henke, R. Schmid, J.-D. Grunwaldt and R. A. Fischer, Flexibility and sorption selectivity in rigid metal-organic frameworks: the impact of ether-functionalised linkers, *Chemistry*, 2010, **16**, 14296–14306.

19 S. Hiraide, Y. Sakanaka, H. Kajiro, S. Kawaguchi, M. T. Miyahara and H. Tanaka, High-throughput gas separation by flexible metal-organic frameworks with fast gating and thermal management capabilities, *Nat. Commun.*, 2020, **11**, 3867.

20 Q. Dong, X. Zhang, S. Liu, R.-B. Lin, Y. Guo, Y. Ma, A. Yonezu, R. Krishna, G. Liu, J. Duan, R. Matsuda, W. Jin and B. Chen, Tuning Gate-Opening of a Flexible Metal-Organic Framework for Ternary Gas Sieving Separation, *Angew. Chem.*, 2020, **59**, 22756–22762.

21 A. He, Z. Jiang, Y. Wu, H. Hussain, J. Rawle, M. E. Briggs, M. A. Little, A. G. Livingston and A. I. Cooper, A smart and responsive crystalline porous organic cage membrane with switchable pore apertures for graded molecular sieving, *Nat. Mater.*, 2022.

22 J. Y. Kim, J. Park, J. Ha, M. Jung, D. Wallacher, A. Franz, R. Balderas-Xicohténcatl, M. Hirscher, S. G. Kang, J. T. Park, I. H. Oh, H. R. Moon and H. Oh, Specific Isotope-Responsive Breathing Transition in Flexible Metal-Organic Frameworks, *J. Am. Chem. Soc.*, 2020, **142**, 13278–13282.

23 E. J. Carrington, C. A. McAnally, A. J. Fletcher, S. P. Thompson, M. Warren and L. Brammer, Solvent-switchable continuous-breathing behaviour in a diamondoid metal-organic framework and its influence on CO2 versus CH4 selectivity, *Nat. Chem.*, 2017, **9**, 882–889.

24 A. Knebel, B. Geppert, K. Volgmann, D. I. Kolokolov, A. G. Stepanov, J. Twiefel, P. Heitjans, D. Volkmer and J. Caro, Defibrillation of soft porous metal-organic frameworks with electric fields, *Science (New York, N.Y.)*, 2017, **358**, 347–351.

25 A. Ghoufi, K. Benhamed, L. Boukli-Hacene and G. Maurin, Electrically Induced Breathing of the MIL-53(Cr) Metal-Organic Framework, *ACS Cent. Sci.*, 2017, **3**, 394–398.

26 J. H. Lee, S. Jeoung, Y. G. Chung and H. R. Moon, Elucidation of flexible metal-organic frameworks: Research progresses and recent developments, *Coord. Chem. Rev.*, 2019, **389**, 161–188.

27 I. Senkovska, V. Bon, L. Abylgazina, M. Mendt, J. Berger, G. Kieslich, P. Petkov, J. Luiz Fiorio, J.-O. Joswig, T. Heine, L. Schaper, C. Bachetzky, R. Schmid, R. A. Fischer, A. Pöppl, E. Brunner and S. Kaskel, Understanding MOF Flexibility: An Analysis Focused on Pillared Layer MOFs as a Model System, *Angew. Chem.*, 2023, **135**.

28 R. Pallach, J. Keupp, K. Terlinden, L. Frentzel-Beyme, M. Kloß, A. Machalica, J. Kotschy, S. K. Vasa, P. A. Chater, C. Sternemann, M. T. Wharmby, R. Linser, R. Schmid and S. Henke, Frustrated flexibility in metal-organic frameworks, *Nat. Commun.*, 2021, **12**, 4097.

29 P. Vervoorts, J. Keupp, A. Schneemann, C. L. Hobday, D. Daisenberger, R. A. Fischer, R. Schmid and G. Kieslich, Configurational Entropy Driven High-Pressure Behaviour of a Flexible Metal-Organic Framework (MOF), *Angew. Chem.*, 2021, **60**, 787–793.

30 J. Wieme, K. Lejaeghere, G. Kresse and V. van Speybroeck, Tuning the balance between dispersion and entropy to design temperature-responsive flexible metal-organic frameworks, *Nat. Commun.*, 2018, **9**, 4899.

31 F.-X. Coudert, Responsive Metal–Organic Frameworks and Framework Materials: Under Pressure, Taking the Heat, in the Spotlight, with Friends, *Chem. Mater.*, 2015, **27**, 1905–1916.

32 P. Vervoorts, J. Stebani, A. S. J. Méndez and G. Kieslich, Structural Chemistry of Metal–Organic Frameworks under Hydrostatic Pressures, *ACS Materials Lett.*, 2021, **3**, 1635–1651.

33 S. Krause, J. D. Evans, V. Bon, S. Crespi, W. Danowski, W. R. Browne, S. Ehrling, F. Walenszus, D. Wallacher, N. Grimm, D. M. Többens, M. S. Weiss, S. Kaskel and B. L. Feringa, Cooperative light-induced breathing of soft porous crystals via azobenzene buckling, *Nat. Commun.*, 2022, **13**, 1951.

34 C. Liu, Y. Jiang, C. Zhou, J. Caro and A. Huang, Photo-switchable smart metal–organic framework membranes with tunable and enhanced molecular sieving performance, *J. Mater. Chem. A*, 2018, **6**, 24949–24955.

35 P. Qin, S. Okur, C. Li, A. Chandresh, D. Mutruc, S. Hecht and L. Heinke, A photoprogrammable electronic nose with switchable selectivity for VOCs using MOF films, *Chem. Sci.*, 2021, **12**, 15700–15709.

36 C. Gao, J. Li, S. Yin, J. Sun and C. Wang, Redox-triggered switching in three-dimensional covalent organic frameworks, *Nat. Commun.*, 2020, **11**, 4919.

37 J. G. M. de Carvalho, R. A. Fischer and A. Pöthig, Molecular Oxygen Activation by Redox-Switchable Anthraquinone-Based Metal-Organic Frameworks, *Inorg. Chem.*, 2021, **60**, 4676–4682.

38 N. Kulachenkov, Q. Haar, S. Shipilovskikh, A. Yankin, J.-F. Pierson, A. Nominé and V. A. Milichko, MOF-Based Sustainable Memory Devices, *Adv. Funct. Mater.*, 2021, 2107949.

39 Z.-Q. Yao, K. Wang, R. Liu, Y.-J. Yuan, J.-J. Pang, Q. W. Li, T. Y. Shao, Z. G. Li, R. Feng, B. Zou, W. Li, J. Xu and X.-H. Bu, Dynamic Full-Color Tuning of Organic Chromophore in a Multi-Stimuli-Responsive 2D Flexible MOF, *Angew. Chem., Int. Ed.*, 2022, **61**, e202202073.

40 P. Serra-Crespo, M. A. van der Veen, E. Gobechiya, K. Houthoofd, Y. Filinchuk, C. E. A. Kirschhock, J. A. Martens, B. F. Sels, D. E. de Vos, F. Kapteijn and J. Gascon, NH2-MIL-53(Al): a high-contrast reversible solid-state nonlinear optical switch, *J. Am. Chem. Soc.*, 2012, **134**, 8314–8317.

41 L. Tom and M. R. P. Kurup, A stimuli responsive multifunctional ZMOF based on an unorthodox polytopic ligand: reversible thermochromism and anion triggered metallogelation, *Dalton Trans.*, 2019, **48**, 16604–16614.

42 P. Freund, I. Senkovska and S. Kaskel, Switchable Conductive MOF-Nanocarbon Composite Coatings as Threshold Sensing Architectures, *ACS Appl. Mater. Interfaces*, 2017, **9**, 43782–43789.

43 L. Chen, W. Zhan, H. Fang, Z. Cao, C. Yuan, Z. Xie, Q. Kuang and L. Zheng, Selective Catalytic Performances of Noble Metal Nanoparticle@MOF Composites: The Concomitant Effect of Aperture Size and Structural Flexibility of MOF Matrices, *Chemistry*, 2017, **23**, 11397–11403.

44 J. Berger, A.-S. Dönmez, A. Ullrich, H. Bunzen, R. A. Fischer and G. Kieslich, Reduced thermal expansion by surface-mounted nanoparticles in a pillared-layered metal-organic framework, *Commun. Chem.*, 2022, **5**.

45 S. Henke, A. Schneemann, A. Wütscher and R. A. Fischer, Directing the breathing behavior of pillared-layered metal-organic frameworks via a systematic library of functionalized linkers bearing flexible substituents, *J. Am. Chem. Soc.*, 2012, **134**, 9464–9474.

46 H. Liu, L. Chang, L. Chen and Y. Li, In situ one-step synthesis of metal–organic framework encapsulated naked Pt nanoparticles without additional reductants, *J. Mater. Chem. A*, 2015, **3**, 8028–8033.

47 S. Henke, A. Schneemann and R. A. Fischer, Massive Anisotropic Thermal Expansion and Thermo-Responsive Breathing in Metal-Organic Frameworks Modulated by Linker Functionalization, *Adv. Funct. Mater.*, 2013, **23**, 5990–5996.

48 J. D. Evans, V. Bon, I. Senkovska and S. Kaskel, A Universal Standard Archive File for Adsorption Data, *Langmuir*, 2021, **37**, 4222–4226.

49 G. Vinai, F. Motti, A. Y. Petrov, V. Polewczyk, V. Bonanni, R. Edla, B. Gobaut, J. Fujii, F. Suran, D. Benedetti, F. Salvador, A. Fondacaro, G. Rossi, G. Panaccione, B. A. Davidson and P. Torelli, An integrated ultra-high vacuum apparatus for growth and in situ characterization of complex materials, *Rev. Sci. Instrum.*, 2020, **91**, 85109.

50 I. Pastoriza-Santos and L. M. Liz-Marzán, N N -Dimethylformamide as a Reaction Medium for Metal Nanoparticle Synthesis, *Adv. Funct. Mater.*, 2009, **19**, 679–688.

51 S. Dai, K. P. Ngoc, L. Grimaud, S. Zhang, A. Tissot and C. Serre, Impact of capping agent removal from Au NPs@MOF core–shell nanoparticle heterogeneous catalysts, *J. Mater. Chem. A*, 2022, **10**, 3201–3205.

52 B. Li, J.-G. Ma and P. Cheng, Integration of Metal Nanoparticles into Metal-Organic Frameworks for Composite Catalysts: Design and Synthetic Strategy, *Small*, 2019, **15**, e1804849.

53 M. J. Thompson, C. L. Hobday, I. Senkovska, V. Bon, S. Ehrling, M. Maliuta, S. Kaskel and T. Düren, Role of particle size and surface functionalisation on the flexibility behaviour of switchable metal–organic framework DUT-8(Ni), *J. Mater. Chem. A*, 2020, **8**, 22703–22711.

54 S. Wannapaiboon, A. Schneemann, I. Hante, M. Tu, K. Epp, A. L. Semrau, C. Sternemann, M. Paulus, S. J. Baxter, G. Kieslich and R. A. Fischer, Control of structural flexibility of layered-pillared metal-organic frameworks anchored at surfaces, *Nat. Commun.*, 2019, **10**, 346.

55 T. D. Bennett, A. K. Cheetham, A. H. Fuchs and F.-X. Coudert, Interplay between defects, disorder and flexibility in metal-organic frameworks, *Nat. Chem.*, 2016, **9**, 11–16.

56 S. Krause, F. S. Reuter, S. Ehrling, V. Bon, I. Senkovska, S. Kaskel and E. Brunner, Impact of Defects and Crystal Size on Negative Gas Adsorption in DUT-49 Analyzed by In Situ129Xe NMR Spectroscopy, *Chem. Mater.*, 2020, **32**, 4641–4650.